https://doi.org/10.5194/egusphere-2025-5825
Preprint. Discussion started: 11 December 2025

# Modeling tsunami and seismic waveforms from regional earthquakes to inform system design and data integration for the Tamtam SMART subsea cable

Kwok Fai Cheung[1], Yoshiki Yamazaki[1], Thorne Lay[2], Matthew J. Fouch[3], John Jr. Niroa[4], and Bruce M. Howe[1]

[1]Department of Ocean and Resources Engineering, University of Hawaii at Manoa, Honolulu, Hawaii, 96822, USA
[2]Department of Earth and Planetary Sciences, University of California Santa Cruz, Santa Cruz, California, 95064, USA
[3]Subsea Data Systems, Washington DC, USA
[4]Vanuatu Meteorology and Geo-hazards Department, Port Vila, Vanuatu

Modelling

*Correspondence to*: Kwok Fai Cheung (cheung@hawaii.edu)

**Abstract.** Science Monitoring And Reliable Telecommunications (SMART) subsea cables utilize and seismic data sensors integrated within repeaters to record temperature, a~~cceleration, and~~ pressure on the seafloor. The planned Tamtam SMART cable will connect Vanuatu and New Caledonia across a major subduction zone. Modeling recent $M_W$ 7.7 to 8.0 earthquakes and maximum considered $M_W$ 8.33 to 8.8 scenarios ~~provides~~ yields a range of seismic waveforms with realistic relative timing and long-period ground displacements at the sensor locations, as well as coseismic seafloor uplift and subsidence at the sources used for tsunami excitation. A non- nonhydrostatic model describes tsunami generation, propagation, and scattering in the southwest Pacific. Spectral analysis of the computed tsunami waves shows multi-scale oscillations along the Vanuatu trench with periods from a few minutes to over an hour. The cable sensor locations are outside energetic antinodes of oscillation modes, and the modeled tsunami amplitude is representative of the seismic source with minor interference from land masses. The suite of synthetic seismic and tsunami waveforms informs the implementation of the sensor system for regional hazard monitoring. The Tamtam SMART cable, deployed in a very active tectonic environment with limited on-land instrumentation, will augment rapid earthquake and tsunami warning as well as source quantification.

## 1. Introduction

The last decade has seen increased interest in leveraging subsea telecommunication cables as a cost-effective means to monitor vast expanses of the ocean. There are currently 1.5 million kilometers of subsea cables in operation around the world. When existing cables are replaced or new routes are planned, sensors can be installed at repeaters or in separate modules, to provide dense measurements of temperature, ~~acceleration, and~~ pressure and seismic data for oceanographic and climate research at a modest incremental cost (Howe et al., 2019). The resulting Science Monitoring And Reliable Telecommunications (SMART) subsea cables can also provide real-time data for earthquake and tsunami early warning, and that has provided motivation for a number of on-going projects, such as the InSEA wet demonstration project off Sicily, Italy; and the Atlantic CAM ring system connecting Lisbon, Azores, and Madeira in Portugal (Howe et al., 2022)[redacted]

Planning for the Tamtam SMART subsea cable between Vanuatu and New Caledonia in the Southwest Pacific is currently underway. The system will stretch across the Vanuatu subduction zone, which is very active and geologically young, with frequent tsunamigenic earthquakes (Roger and Pelletier, 2024). The planned cable route extends from Port Vila, the capital of Vanuatu, ~~on~~ to Efate Island, along the archipelago to the south, before crossing the trench to reach an existing landing station on Lifou Island with connectivity to the rest of New Caledonia (Fig. 1). There are four sensor modules 50~90 km apart along the 450 km cable. Three sensor modules are planned for the upper margin slope along the shelf edge and one at the trench to provide real-time earthquake and tsunami monitoring capability near populated areas. This project is situated in a region with existing seismic and sea level networks that can provide information for examination of data quality and interoperability. As shown in Fig. 1a, the New Zealand DART (Detection and Reporting of Tsunami) network has some coverage of tsunami waves in the Southwest Pacific with stations to the west and south of the Vanuatu islands (Fry et al., 2020). Global seismic network stations are rather sparsely distributed in the Southwest Pacific but are supplemented by more than 50 stations of the Oceania Regional Seismic Network (ORSNET) operated by South Pacific countries (UNESCO-IOC, 2025).

Tsunamis in the region have been generated predominantly by earthquakes with volcanic and non-seismic sources representing less than 5% of documented events (Roger and Pelletier, 2024). Fig. 1b shows the locations of selected tsunamigenic earthquakes with regional implications. The northern Vanuatu subduction zone has produced several large earthquakes in the past century. One of the largest is the 6 February 2013 $M_W$ 8.0 Santa Cruz Islands thrust faulting with shallow eastward dip that generated a destructive tsunami impacting local communities (e.g., Lay et al., 2013; Cleveland et al., 2014). Across the d'Entrecasteaux Ridge, the southern Vanuatu subduction zone is known for strong and long-duration aftershock sequences (Ye et al., 2021), accompanying major plate boundary and outer rise earthquakes (Roger et al., 2021). The largest, 1875 thrust-faulting earthquake with an estimated *Mw* 8.1-8.2 produced sediment deposits reaching 10 m elevation on the northeastern coast of Lifou Island, + space New Caledonia (Paris et al., 2023), while an *Mw* 7.7 normal faulting event in May 1995 along the Loyalty ridge generated a tsunami with 8 m runup on Aneityum Island, Vanuatu (Roger and Pelletier, 2024).

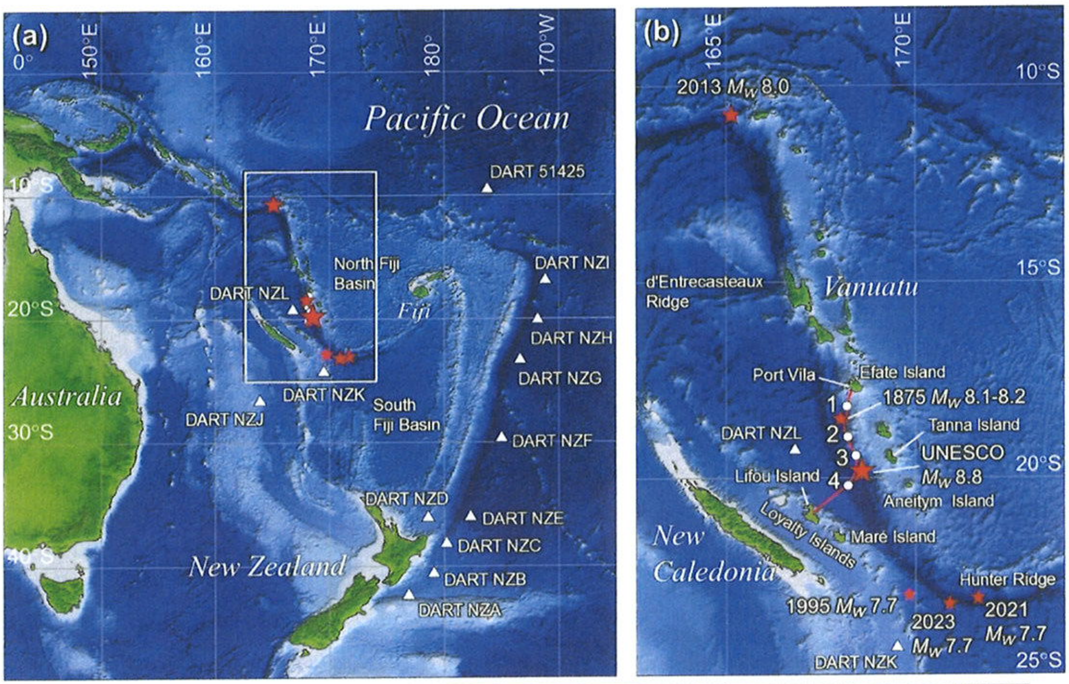

**Figure** the **1.** Location map and two levels of nested computational grids. (a) Level-1 Southwest Pacific. White rectangle indicates the level-2 grid coverage. (b) Level-2 Vanuatu subduction zone. The magenta line and white circles denote planned SMART cable and sensor locations. White triangles denote DART locations. Smaller red stars indicate epicenters of large historical and recent tsunamigenic earthquakes and the large red star indicates the maximum earthquake in the Southern Vanuatu Subduction Zone from UNESCO-IOC (2025).

The southernmost Vanuatu Trench curves eastward along the Hunter Ridge. The two largest *Mw* 7.7 earthquakes in the past quarter-century occurred on opposing sides of the Southern Vanuatu Trench in 2021 and 2023. The resulting tsunamis of similar wave amplitude have distinct near-field patterns associated with the source location in relation to nearby seamounts and islands, but similar far-field patterns due to standing waves amongst the many seamounts and islands in the southwest Pacific (Robert et al., 2025). This event pair within 2 years is analogous to the 2013 Santa Cruz megathrust $M_W$ 8.0 and 2015 normal faulting $M_W$ 7.0 earthquakes on opposing sides of the trench in the northern Vanuatu subduction zone (Heidarzadeh et al., 2016). These recent earthquakes at the northern and southern termini of the subduction zone produced moderate tsunamis affecting Vanuatu and New Caledonia. Larger historical earthquakes between the two island chains, such as the 1875 $M_W$ 8.1-8.2 and the 1995 $M_W$ 7.7, indicate greater tsunami risk to population centers. Port Vila was extensively damaged by ground shaking from a nearby 54 km deep $M_W$ 7.3 intraslab event in December 2024, accompanied by a minor tsunami of 0.25 m amplitude.

Governments, scientists, and stakeholders are motivated to understand earthquake and tsunami hazards to support comprehensive risk management strategies among nations in the Southwest Pacific. UNESCO-IOC (2025) proposed maximum earthquake scenarios inferred probabilistically from the estimated degree of segmentation, the width of strain accumulation zones, and fault locking relative to plate convergence, and the material properties of rocks along the Vanuatu subduction zone. Comparable maximum earthquake estimates were made for the northern, central, southern, and Matthew-Hunter Islands regions along the arc. Full rupture of the southern 500-km long segment, where the proposed Tamtam SMART cable is located, can produce up to $M_W$ 8.8 involving five $M_W$ 8.33 subevents. These scenarios along with the well-resolved 2013 $M_W$ 8.0 Santa Cruz Islands earthquake to the north and the 2021 and 2023 $M_W$ 7.7 earthquakes southeast of the Loyalty Islands provide a range of large events in the region that the proposed SMART subsea cables might record signals for (Fig. 1b). Modeling the corresponding earthquake and tsunami signals can inform system and sensor design, aid data integration into regional networks, and identify implications for emergency management in the cable system planning stage.

## 2. Tsunami and seismic wave modeling

Finite fault-slip models have been an effective tool to describe earthquake rupture and seafloor deformation time histories for non-hydrostatic modeling of tsunami generation (Yamazaki et al., 2023). The methodology has evolved over the last half-century from simple point source models in a homogeneous, elastic half-space to space-time distributions of slip over a finite-fault surface or network of surfaces, constrained by combinations of seismic, geodetic, and tsunami observations.

Such models are now routinely obtained for large earthquakes, and can be used in quantitative forward modeling of long-period ground motions at any location of interest.

### 2.1 Rupture models

Finite fault-slip models describe rupture kinematics through grids of subfaults, each of which has uniform slip and a parameteri~~z~~sed source time function. The collective motion accounts for the spatial-temporal seismic moment and energy release during the rupture. In our present formulation, the seafloor vertical displacement is computed from the half-space solution of Okada (1985) and adjusted for horizontal translation of the local slope according to Tanioka and Satake (1996). Fig. 2 shows the finite fault-slip models and co-seismic vertical seafloor displacement for the 2013 $M_W$ 8.0 Santa Cruz Islands earthquake (Lay et al., 2013), the 2021 and 2023 $M_W$ 7.7 earthquakes southeast of the Loyalty Islands (Robert et al., 2025), and the $M_W$ 8.8 maximum is considered earthquake scenario for the southern Vanuatu subduction zone (UNESCO-IOC, 2025). The three historical events have finer subfaults that provide fairly detailed slip distributions and time histories inferred from global seismic and regional tsunami wave recordings, valid for seismic periods longer than ~5-10 s. The maximum earthquake scenario has larger subfaults with prescribed uniform slip and rise time, and is only valid for seismic periods longer than ~15 s.

The 2013 $M_W$ 8.0 Santa Cruz Islands earthquake has a shallow eastward dip in two large slip patches and a southeastward rupture expansion at ~1.5 km/s. The megathrust rupture has up to 12.7 m slip producing 3.3 m near-trench uplift and minor arc subsidence (Lay et al., 2013). The 2021 $M_W$ 7.7 thrust-faulting earthquake occurred at the plate boundary interface near the southern hook of the Vanuatu subduction zone. The peak slip reaches 7.5 m over a 55 s rupture time and produces 1.3 m uplift and minor subsidence on the lower and upper margin slope (Robert et al., 2025). The nearby 2023 $M_W$ 7.7 earthquake with a similar east-west extent involved a normal fault in the outer rise. The peak slip reaches 5.2 m over a 45 s rupture time with relatively small uplift but a large subsidence of 2.4 m near the trench (Robert et al., 2025). The finite fault models for the three historical events, which have been determined from joint seismic and tsunami modeling, are implemented to provide time histories of seafloor deformation for tsunami excitation directly. Short-period features of the sources and details of the propagation structures are not known, so we restrict our seismic modeling near the Tamtam sites to ground displacements with long-periods consistent with simplified, point-source model representations in a one-dimensional velocity structure.

https://doi.org/10.5194/egusphere-2025-5825
Preprint. Discussion started: 11 December 2025

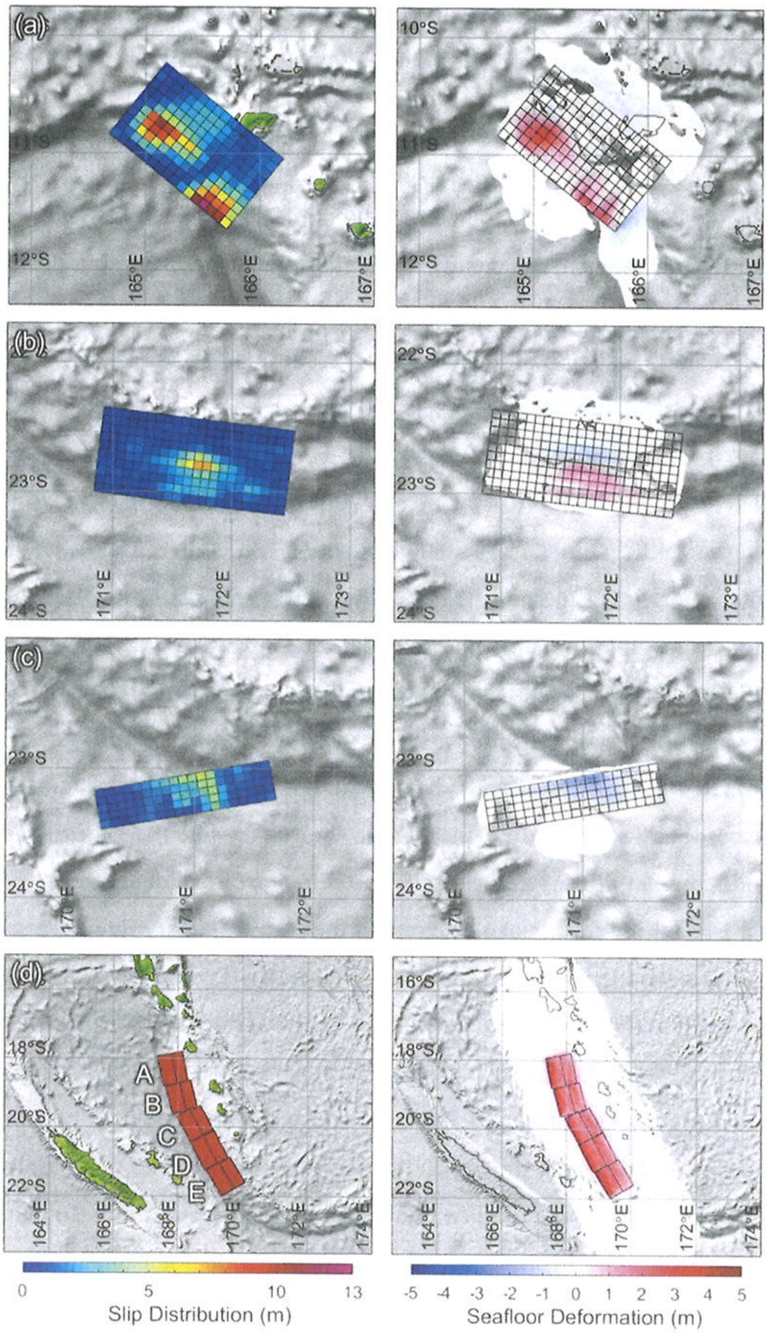

**Figure 2.** Slip distribution and seafloor deformation. (a) The 2013 $M_W$ 8.0 Santa Cruz Islands earthquake. (b) The 2021 $M_W$ 7.7 earthquake southeast of the Loyalty Islands. (c) The 2023 $M_W$ 7.7 earthquake southeast of the Loyalty Islands. (d) UNESCO $M_W$ 8.33 A, B, C, D, and E sub-events which combine to give the $M_W$ 8.8 earthquake scenario.

The rupture of the maximum considered earthquake scenario extends 500 km along the southern Vanuatu subduction zone and 100 km downdip from the trench (UNESCO-IOC, 2025). The $M_W$ 8.8 earthquake scenario corresponds to the 90th percentile in the posterior maximum moment distribution of the probabilistic tsunami hazard assessment compiled by Davis and Griffin (2018). The model has uniform slip of 10 m and a rigidity of 40 GPa. The slip is within the range of the three recent major events from 5.2 to 12.7 m, but is implemented over a much larger area for the maximum scenario. The uplift varies gradually from 1.1 m at the shelf edge to 4.6 m near the trench and the subsidence is relatively small due to the uniform slip across the full segment. The five $M_W$ 8.33 subevents on 100 km wide and 100 km long ruptures can be considered separately as local failures along the segment to augment the parameter space. Each subevent is comparable to the largest observed, 1875 $M_W$ 8.1-8.2 earthquake in the region (Ioualalen et al., 2017). For the modeling of tsunami excitation, the rupture is assumed to start simultaneously across the entire fault and the dislocation follow~~s~~ a linear ramp function over a 30 sec rise time to reach the specified total slip. There is no known constraint on rupture heterogeneity or directivity. Simultaneous rupture of the five subevents is computed for the $M_W$ 8.8 earthquake scenario to direct tsunami waves normal to the arc and to provide a conservative estimate of the resulting impact ~~to~~ on local communities on either side.

## 2.2 Tsunami modeling

The tsunami code NEOWAVE augments the commonly used nonlinear shallow-water equations with depth-averaged vertical velocity and non-hydrostatic pressure (Yamazaki et al., 2009, 2011). The resulting quasi three-dimensional flow can describe tsunami generation from time-dependent seafloor deformation, frequency dispersion during trans-oceanic propagation, and wavenumber-dependent shoaling on seafloor slopes. The vertical inertia in the nonhydrostatic formulation facilitates an accurate description of sea-surface oscillation at tsunami sources as well as runup and drawdown on steep topography (Bai et al., 2023). A shock-capturing scheme approximates breaking waves as bores or hydraulic jumps to ensure conservation of mass and momentum while enabling energy dissipation without predefined empirical mechanisms. These model capabilities have been benchmarked against mathematical and numerical models as well as laboratory and field measurements (Yamazaki et al., 2023).

The modeling involves two levels of two-way nested computational grids, telescoping from the Southwest Pacific to the tsunami source region along the Vanuatu subduction zone. The digital

https://doi.org/10.5194/egusphere-2025-5825
Preprint. Discussion started: 11 December 2025

elevation model is derived from GEBCO14 at 30 arcsec (~0.9 km). The level-1 grid covers the Southwest Pacific to capture large-scale standing waves generated by reflection from land masses as well as trapping along island chains (Fig. 1a). The 2-arcmin (~3.7 km) resolution leads to optimal model dispersion for transoceanic tsunami propagation (Li and Cheung, 2019). As shown in Fig. 1b, the level-2 grid extends along the Vanuatu subduction zone and resolves the margin and tsunami sources at 30 arcsec (~0.9 km). The co-seismic seafloor vertical displacement defines the tsunami excitation and updates the digital elevation model. Inundation is not modeled at this resolution and the subgrid roughness of the seafloor is described by a Manning's number of 0.025. The local mean-sea level is the datum of the digital elevation model as well as the sea surface elevation.

### 2.3 Seismic wave modeling

Dynamic ground motions are computed at a target location (18.782°S, 168.2°E), which is planned for sensor 2 on the Tamtam SMART cable (Fig. 1b). The predicted ground motions vary slowly in space and thus remain very similar at the four sensor locations. The purpose here is to inform sensor design and data integration by estimating approximate timing, duration, and levels of long period ground displacement produced near the site for a large recent plate boundary and plausible maximum regional ruptures along the Vanuatu subduction zone. The precise details of the historical, finite-fault ruptures are not important here and are unknown for the maximum rupture scenarios. Numerical modeling is thus simplified to the computation of an equivalent point-source representations of the three large recent events and the subevents of the maximum rupture scenario along with their composite.

Synthetic seismograms are computed using a standard one-dimensional Earth Model, which is an anisotropic version of the Preliminary Reference Earth Model (PREM; Dziewonski and Anderson, 1981). The ground displacements up to 2 s period are computed using the SYNGINE (synthetic engine) seismic wave simulator (https://ds.iris.edu/ds/products/ondemandsynthetics/), for point-source moment tensor representations of the earthquake models. While short-period seismic waves and associated ground velocities and accelerations will be affected by the actual three-dimensional structure along the paths from sources to the observing location, the details are not known for this particular assessment of the ground shaking levels. Our focus is on the relative timing, duration, and amplitude of long period ground displacements produced by each source near the Tamtam site.

## 3. Model results

The modeling work provides tsunami and seismic waves generated by the three recent major earthquakes and the UNESCO maximum scenario, including its five subevents along the Vanuatu subduction zone. The tsunami modeling covers an elapsed time of 10 hours to capture the shelf oscillations along the archipelago as well as standing waves within the north and south Fiji Basins. The results include regional tsunami amplitude maps, energetic oscillation modes along the margin, and synthetic tsunami and seismic waveforms at the representative, sensor 2 location of the planned SMART subsea cable.

### 3.1 Recent major events

The 2013 *Mw* 8.0 Santa Cruz Islands earthquake and the 2021 and 2023 *Mw* 7.7 earthquakes southeast of the Loyalty Islands are representative of major events from the northern and southern termini of the Vanuatu subduction zone. Fig. 3 shows the regional distributions of the maximum sea surface excursion, which includes crest and trough amplitude to better represent the energy pattern, especially for the 2023 normal-fault event (Robert et al., 2025). The two near-trench uplift patches from the 2013 thrust faulting, provides the primary source of the tsunami with minor contributions from subsidence on the upper margin slope (Fig. 2a). Constructive interference of the radiated waves from the two uplift patches define~~s~~ the main lobes in the northeast and southwest directions away from Vanuatu (Fig. 3a). Refraction of the radiated waves over the margin slope and outer rise produces notable side lobes to the east and south toward the Santa Cruz Islands and the main island of New Caledonia, respectively. The SMART cable site located southeast of the source on the margin slope experiences only minor wave action albeit with amplification over adjacent insular shelves along the Vanuatu Islands.

The 2021 and 2023 *Mw* 7.7 earthquakes on opposing sides of the southern Vanuatu Trench have similar east-west rupture extents~~,~~ but produce tsunamis with a leading crest and a leading trough associated with the thrust and normal faulting mechanisms, respectively (Robert et al., 2025). The distinct northern energy lobes result from the source location relative to seamounts and islands immediately north of along the Hunter Ridge. In comparison, the southern lobes are normal to the strike of the respective earthquakes due to the lack of major bathymetric features south of the source. The 2023 earthquake has narrower seafloor deformation beneath deeper water resulting in shorter period tsunami waves that are focused more effectively along seamounts and island chains to produce a more elaborate wave pattern. Both tsunamis generated by earthquakes in the southern arc of the subduction zone direct the primary energy to the north and south, with minimal threat to the main island of New Caledonia. Refraction of the radiated waves over the margin slope generates side lobes toward the Vanuatu Islands with moderate wave action associated with the shelf oscillations for both events.

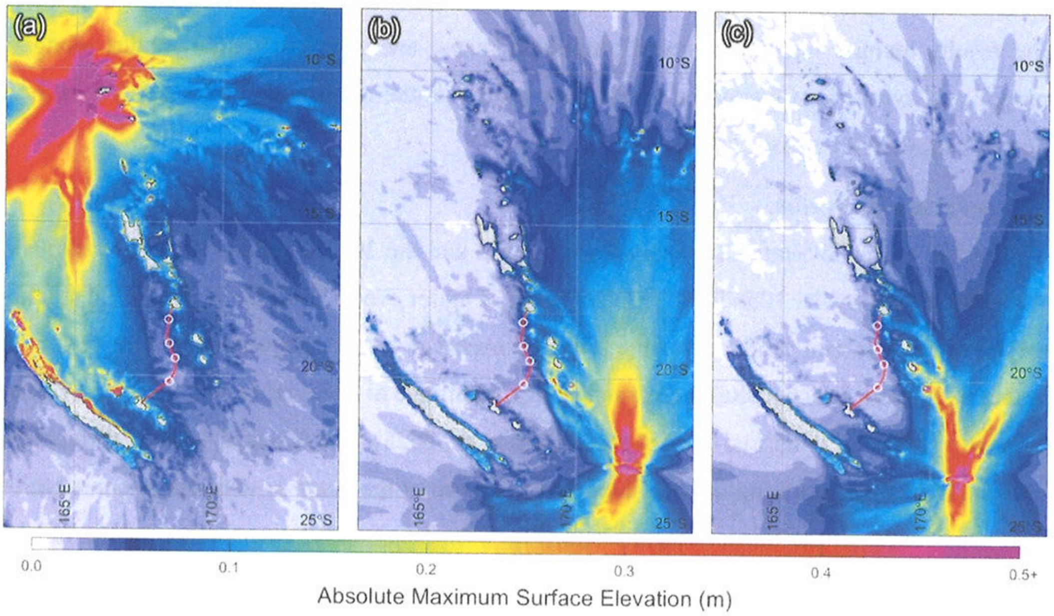

**Figure 3.** Computed absolute maximum surface elevation of tsunamis generated by recent major earthquakes. (a) The 2013 $M_W$ 8.0 Santa Cruz Islands earthquake. (b) The 2021 $M_W$ 7.7 Southeast of the Loyalty Islands earthquake. (c) The 2023 $M_W$ 7.7 Southeast of Loyalty Islands earthquake. Red line and circles denote planned SMART cable and sensor locations.

The four planned sensor modules are located off the insular shelves (Fig. 1b) and outside zones of tsunami amplification for all three recent events (Fig. 3). The computed sea-surface elevations at the sensors are an order of magnitude smaller compared to the adjacent shallow shelves. The bathymetry-driven oscillation is illustrated by spectral analysis of the computed 2013 tsunami that converts the surface elevation time history to amplitude as a function of period (Munger and Cheung, 2008). Fig. 4 shows selected oscillation modes with well-defined nodal lines, where the amplitude is zero, and the phase varies by 180° across, indicative of resonance. The 7 to 40-min modes indicate distinct standing edge waves along the New Caledonia ridge, the Loyalty Island ridge, and the Santa Cruz and Vanuatu Islands. The standing waves along the geographically smaller, Loyalty Island ridge vanishes for longer-period oscillations at the margin and basin scales. Since the oscillation modes are independent of tsunami sources (e.g., Cheung et al., 2013; Aranguiz et al., 2019), the SMART sensors located mostly outside energetic antinodes can record direct tsunami signals with minor influences from adjacent landmasses.

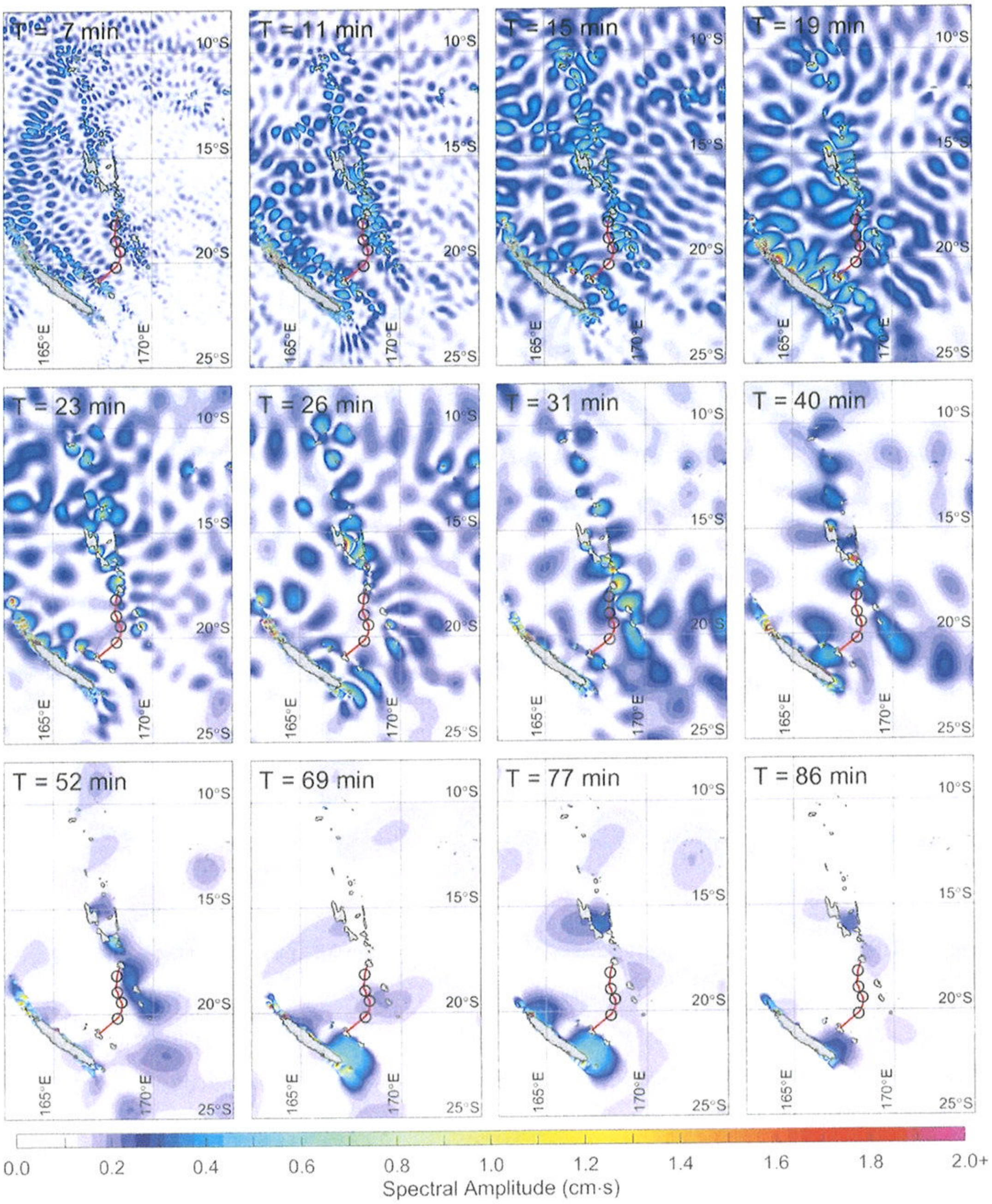

**Figure 4.** Oscillation modes derived from the 2013 $M_W$ 8.0 Santa Cruz tsunami. Red line and circles denote planned SMART cable and sensor locations.

Fig. 5 shows the computed waveforms and spectra from the 2013, 2021, and 2023 tsunamis at sensor 2. All three tsunamis arrive in ~1 hr after earthquake initiation. The 2013 and 2021 thrust faulting events produce initial arrivals in the form of a crest, while the 2023 normal faulting results in a leading trough. The initial arrivals directly from the source via the Vanuatu trench are weak for the 2021 and 2023 events southwest of the Loyalty Islands, because the energy is diverted into the North Fiji Basin through refraction-diffraction across the Hunter Ridge (Robert et al., 2025). The subsequent waveforms are primarily leaked energy from nearby shelf oscillations, where the amplitude is an order of magnitude larger (Fig. 3). The 2013 tsunami from the San Cruz Islands has more energetic long period components due to the sensor's location at 90° azimuth from the main lobe. Despite the varying waveforms in the three events, their spectra show similar sets of harmonics with periods in 10~40 and 50~100 min associated with the island and basin-scale oscillations as shown in Fig 4.

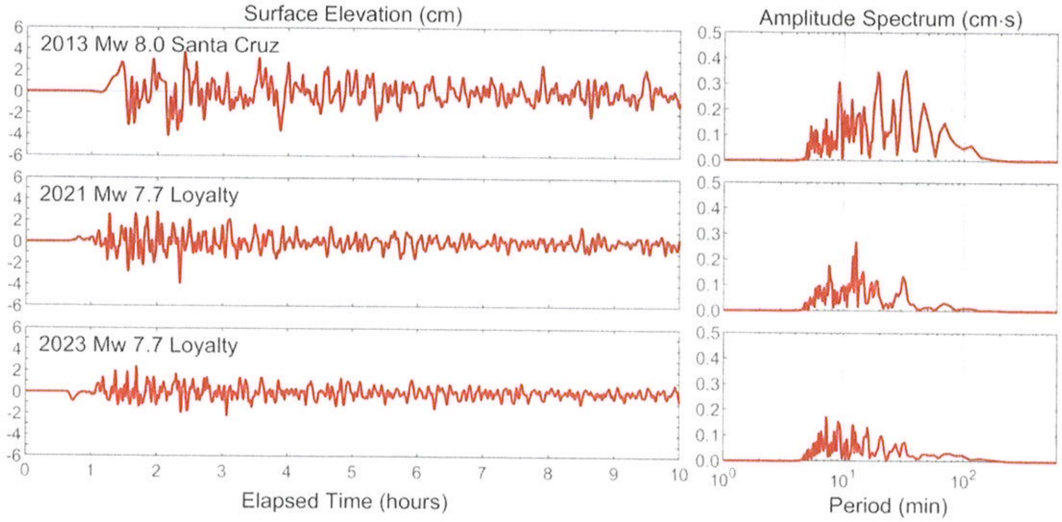

**Figure 5.** Synthetic tsunami time series and spectra at the target location of SMART sensor 2 from the three recent major earthquakes in the Vanuatu subduction zone shown in Fig. 2a-c.

The vertical and transverse (horizontal perpendicular to the great circle path at the receiver) ground displacements at sensor 2 of the SMART cable are computed for point-source representations of the three major recent ruptures along the Vanuatu subduction zone (Fig. 6). A 15-s low-pass filter has been applied to approximately account for the temporal finiteness of the ruptures. The arrival times vary with distance from the source to the observing point. Peak ground motions of about 0.2 m are associated with the large Rayleigh wave and Love wave packets on the vertical and transverse components, respectively. The signals include all body wave arrivals. The initial P wave arrives at about 75-120 s after the origin time, when real-time analysis of ground shaking detected at the cable could commence. With a distribution of 4 three-component sensors along the cable, if on-scale recordings are obtained, rapid array processing could determine the azimuth of approach, and initial ground motion amplitudes can be used for magnitude estimation. Surface wave analysis of the larger signals is viable within 150 to 380 s of the earthquake origin time, if low frequency signals are recorded. With tsunami arrivals also varying with the source distance, a rapid tsunami potential assessment could be commenced using the Tamtam cable observations along with regional and global network observations.

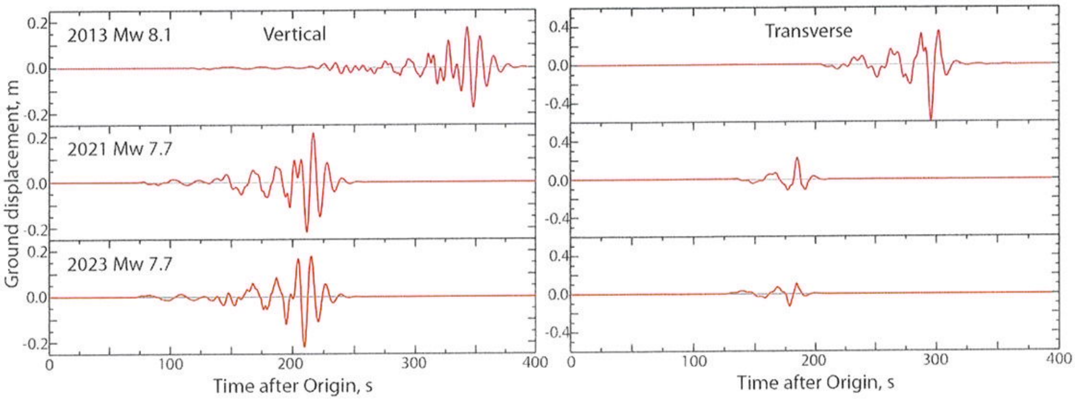

**Figure 6.** Synthetic ground displacement time series at the target location of SMART sensor 2 from three recent major earthquakes in the Vanuatu subduction zone shown in Fig. 2a-c.

### 3.2 UNESCO scenarios

The UNESCO $M_W$ 8.8 maximum earthquake scenario and its five $M_W$ 8.33 subevents complement the historical events to provide more complete coverage of the parameter space, especially along the most critical southern segment adjacent to population centers. Fig. 7 shows the tsunami wave amplitude along the Vanuatu subduction zone for the six scenarios. The initial wave of the thrust-faulting events is characteri~~z~~sed by sea-surface uplift across the margin slope reaching 3.7 m near the trench. Subevent A at the northern end of the segment has the most severe impact ~~to~~ on Vanuatu with waves reaching 8.5 m elevation at the east-facing shore of Efate Island, while subevents to the south are more critical to the Loyalty Islands with a maximum elevation of 9.3 m at Maré Island (Fig. 7). For the combined $M_W$ 8.8 scenario, the arc curvature focuses the energy toward the southern Vanuatu Islands with nearshore amplification to 11.5 m elevation at

https://doi.org/10.5194/egusphere-2025-5825
Preprint. Discussion started: 11 December 2025

Tanna Island. The computed water elevation reaches 12.7 and 11.9 m at Lifou Island and the main island of New Caledonia. Since these values are surface elevations at the shore, resolvable by the 0.5 arcmin (0.9 km) grid, runup heights might be larger or smaller depending on the coastal terrain.

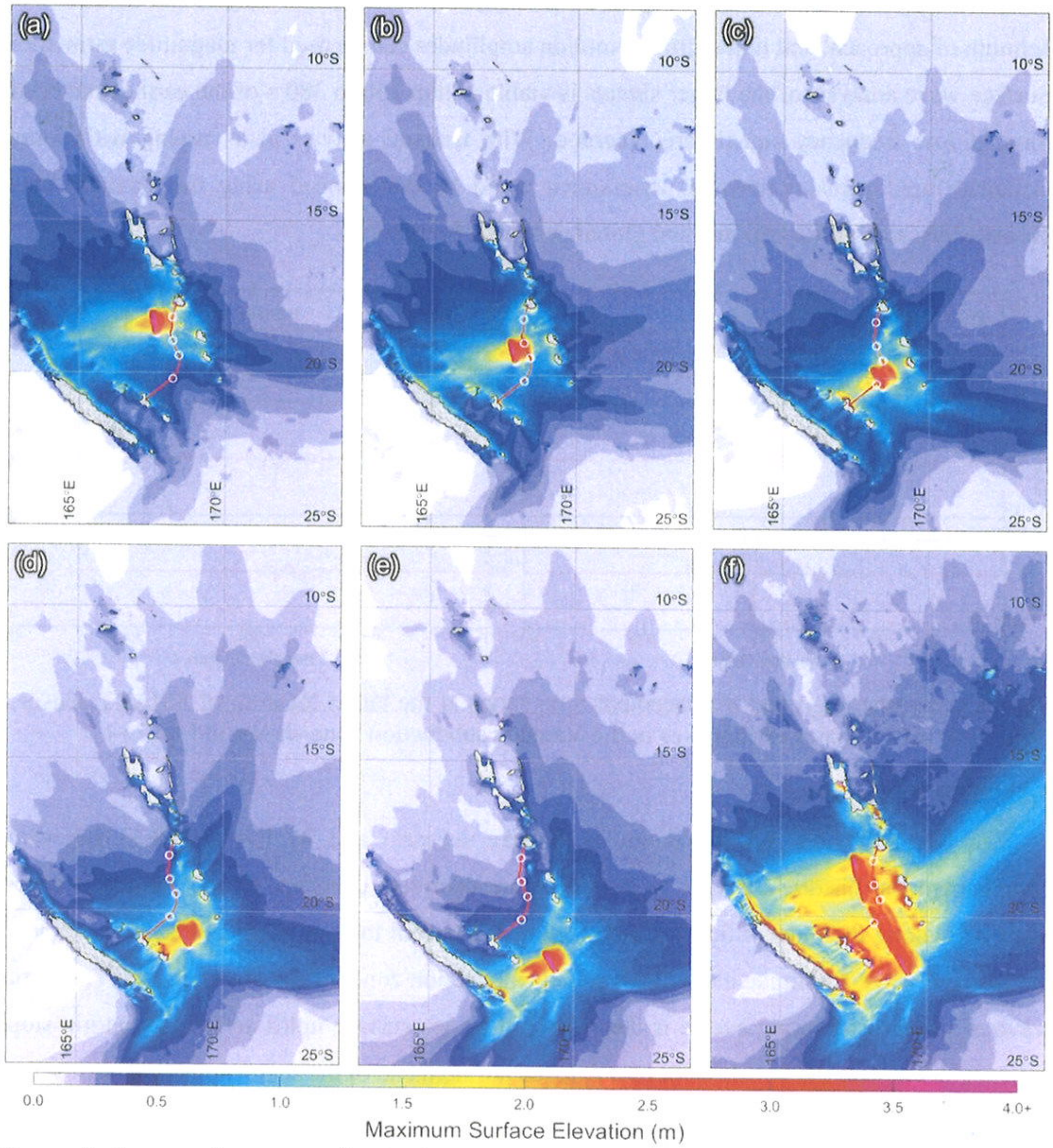

**Figure 7.** Computed wave amplitude of tsunamis generated by UNESCO earthquake scenarios in Figure 2d. (a) $M_W$ 8.33 A earthquake. (b) $M_W$ 8.33 B earthquake. (c) $M_W$ 8.33 C earthquake. (d) $M_W$ 8.33 D earthquake. (e) $M_W$ 8.33 E earthquake. (f) $M_W$ 8.8 combined maximum earthquake scenario. Red line and circles denote planned locations of the SMART cable and sensors.

https://doi.org/10.5194/egusphere-2025-5825
Preprint. Discussion started: 11 December 2025

At least one SMART sensor will be located within the tsunami source regions of subevent~~s~~ A through C as well as the combined event with immediate signature of the initial sea surface uplift. An analysis of the model data shows travel times of 11 and 18 min for the tsunamis sourced from subevents D and E to reach the nearest sensor. Fig. 8 shows the computed waveforms and spectra at sensor 2 from the five subevents and the combined scenario for illustration. The sea surface rises to 2.5 m during the rupture of subevent B directly beneath the sensor, and with only minor energy trapping or resonance over the margin slope, the oscillation subsides rapidly through radiation. Even with rapid wave attenuation outside the source region, the sensor registers direct tsunami signals with less than 1 m amplitude for the other subevents. The combined event has an initial wave amplitude similar to subevent B, but the much larger rupture length results in stronger codas due to waves arriving sequentially from the five subevents along the segment. The wave spectra for all six scenarios show strong bimodal, island and basin-scale excitations with peaks closely aligned with the oscillation modes deduced from the 2013 Santa Cruz Island event (Fig. 4).

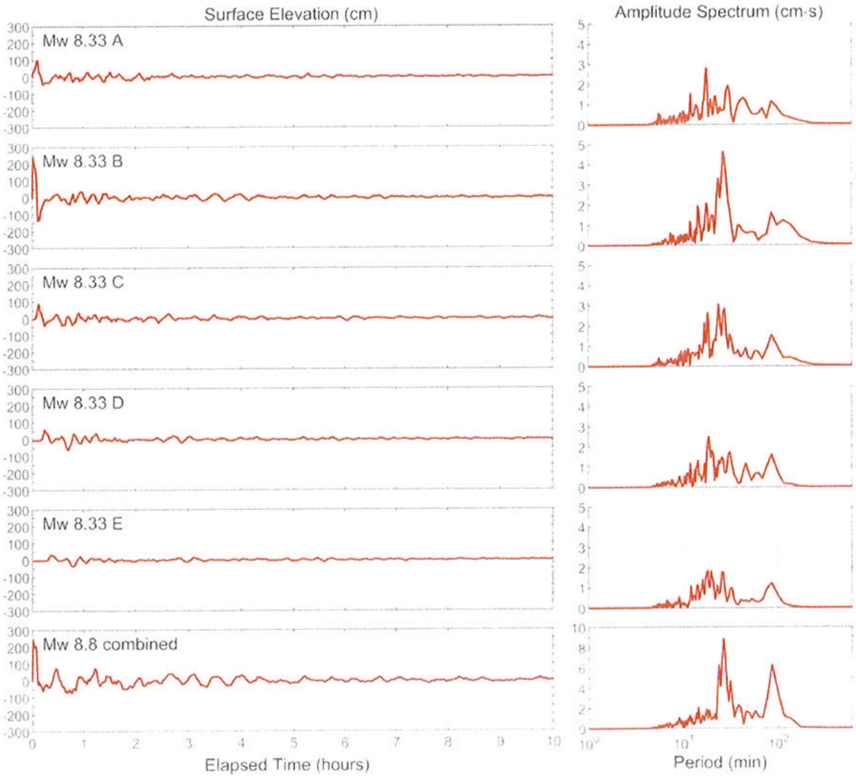

**Figure 8.** Synthetic tsunami time series and spectral at the target location of SMART sensor 2 for the UNESCO earthquake scenarios shown in Fig. 2d.

The seismic waves at the sensor 2 location are computed for the individual $M_W$ 8.33 subevents and the $M_W$ 8.8 combined faulting. All scenarios involve a 10 m slip with a moment tensor point sources at subevent centers and synchronous rupture of the entire segment for simplicity. Fig. 9 shows the subevent signals comprising complete seismic ground motions, as well as static displacements. A low-pass filter with a 15 s corner has been applied to approximately account for the expected smoothing over the subevent space-time extent. Ground motions are shown for the vertical and transverse components and the time variations between arrivals indicate the distance from subevent centers to the sensor. The strongest seismic waves are produced by subevent B directly beneath the sensor with peak vertical and transverse transient displacements reaching 7 m as well as a static transverse displacement of ~1 m after passage of the large surface waves.

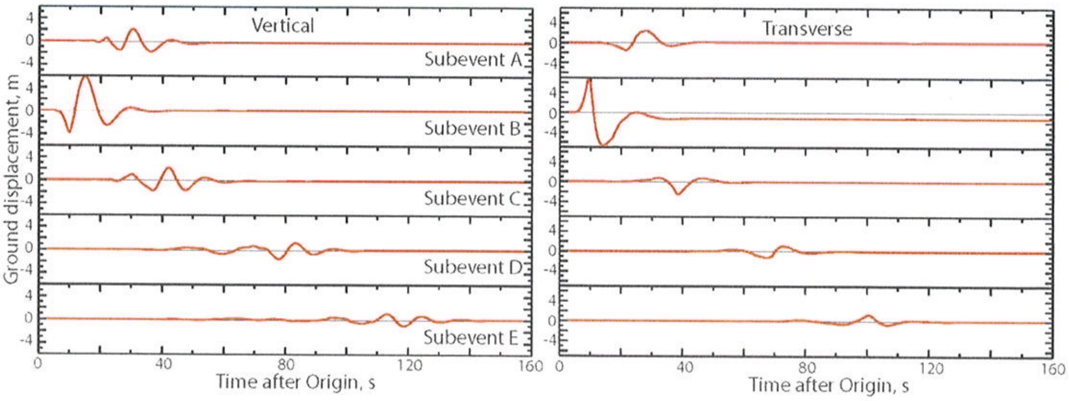

**Figure 9.** Synthetic ground displacement time series at the target location of SMART sensor 2 for the UNESCO $M_W$ 8.33 earthquake scenarios A-E in Fig. 2d. A point-source at the center of each subfault is used for the calculations, and the displacements are low-pass filtered at 15 s period to account for slip duration over the subevent. Vertical and transverse (orthogonal to the great-circle connecting the source and sensor locations) ground displacements are shown.

The composite, long duration displacement for the $M_W$ 8.8 earthquake scenario is shown in Fig. 10. Since the subevents are assumed to rupture at the same time, their arrivals are delayed by propagation distance alone. The composite ground motions are expressed in terms of the vertical, north-south, and east-west components because the transverse component changes with each subevent location. A 15-s low-pass filter is again applied to approximately account for finiteness of the individual subevents. The sequence of discrete subevent pulses would be smeared out for a true continuous rupture, but the heterogeneous coupling expected along the subduction zone would likely involve correspondingly complex localized failures. The peak ground motion is about 6 m on the vertical and 7.5 m on the horizontal components along with appreciable static displacements due to the sensor location in the rupture zone.

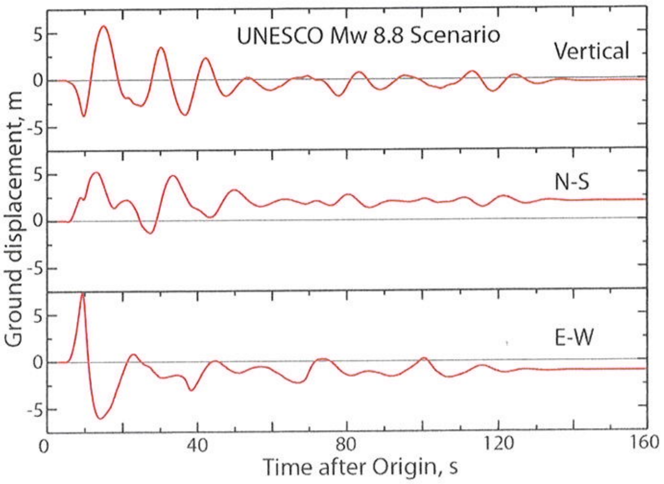

**Figure 10.** Synthetic ground displacement time series at the target location of SMART sensor 2 for the UNESCO $M_W$ 8.8 earthquake scenario in Fig. 2d. For simplicity, the 5 subevents are assumed to rupture synchronously, and the summed displacements are shown for the vertical, north-south, and east-west components of motion due to the changing geometry relative to the target location. A low pass filter at 15 s has been applied.

## 4. Discussion and Conclusions

Large earthquakes occur along the entire Vanuatu subduction zone exposing many islands in the region to strong ground shaking and tsunami wave impact. Prior studies have systematically examined the hazards and developed fault models for recent major earthquakes and maximum events. These fault models form a basis to develop a plausible range of seismic and tsunami waveforms expected at the Tamtam SMART cable. The results provide a reference for hazard assessment, system and data integration, and emergency management.

### 4.1 Earthquake and tsunami hazards

There have been 18 shallow (< 70 km deep) $M_W$ 7.5+ earthquakes recorded in the Vanuatu subduction zone since 1900 (Cleveland et al., 2014; UNESCO-IOC, 2025). The UNESCO maximum scenario of $M_W$ 8.8 provides an upper-bound estimate of potential ground motions and tsunami impacts, but a far-smaller, more frequent major event in the southern segment can still devastate local communities in Vanuatu and New Caledonia. For example, the tsunami generated by the 1875 $M_W$ 8.1-8.2 earthquake produced sediment deposits reaching 10 m elevation on the

https://doi.org/10.5194/egusphere-2025-5825
Preprint. Discussion started: 11 December 2025

northeastern coast of Lifou Island, New Caledonia (Paris et al., 2023). The impact is comparable to the UNESCO subevents of $M_W$ 8.33 with computed sea-surface elevation reaching 8.5 and 9.3 m at the shore of Efate Island and Maré Island in Vanuatu and New Caledonia. A recent 17 December 2024 $M_W$ 7.3 earthquake located 24 km west of Port Vila took 14 lives and injured 265, producing extensive damage in the capital of Vanuatu and long-term impacts on the tourism industry (World Bank, 2025). This event was 54 km deep within the subducting slab, but still produced a 25 cm tsunami. The depth and proximity of such an event to the island leaves little warning times for seismic or tsunami wave arrivals either with or without the Tamtam cable.

A major event from the northern or Matthew-Hunter segment, such as the 2013 $M_W$ 8.0 and 2021 and 2023 $M_W$ 7.7 ruptures, also pose~~s~~ earthquake and tsunami hazards in Vanuatu and New Caledonia. The resulting tsunami arrives at the cable locations within an hour after the earthquake allowing limited time to respond if deemed destructive. Hazardous ocean conditions can be long lasting due to amplification and trapping of tsunami energy along island chains (Cheung et al., 2013). The resulting surges might damage ships and disrupt harbor operations despite having minor inundation risks. The limited number of regional seismic and geodetic sensors in operation hampers earthquake and tsunami warning capabilities along the entire subduction zone. The deployment of continuous monitoring along the Tamtam cable may contribute substantially to regional event detection and rapid assessment, particularly along the southern Vanuatu subduction zone.

### 4.2 Sensor system and data

The seismic, pressure, and temperature sensors are installed inside the repeater housing or in separate modules of submarine telecommunication cables in the case of Tamtam. The broadband seismic sensors and optional accelerometers will be provided by Nanometrics (https://nanometrics.ca), and the temperature and pressure sensors will be supplied by RBR (https://rbr-global.com). The fabrication of sensor modules will be integrated into the cable manufacturing process by Alcatel Submarine Networks (ASN) through its Climate Change Nodes initiative. The collected data from the Tamtam SMART cable will be provided via ASN's Climate Change Portal for low-latency distribution to hazards monitoring agencies, such as the Vanuatu Meteorological and Geohazards Department (VMGD), Oceania Regional Seismic Network (ORSNET), and for long-term storage and dissemination for further analysis and climate research via Ifremer (French Research Institute for Exploitation of the Sea).

With tsunami waves arriving well after seismic waves, a rapid tsunami potential assessment could be commenced using the cable seismic observations along with regional and global land-based seismic network records. The spectral analysis has shown the recorded tsunami~~s~~ signals from sensors placed outside insular shelves have minor effects from resonance oscillations to provide general indications of potential impact and confirm inferences from seismic observations. Caution must be exercised for earthquake sources near the sensors. Large dynamic ground displacement might interfere with the operations of motion sensors laid on sediments. Lacking specific knowledge of the short-period ground displacements and the associated ground velocities and accelerations, we do not attempt to predict the actual recording fidelity of the Tamtam sensors, but after deployment, ground motion models can quickly be developed for the paths around the stations. Also not considered in this study is seismic noise in water level records that might mask the initial tsunami arrivals as commonly seen in bottom pressure data from DART stations near the earthquake sources (e.g., Bai et al., 2022, 2023). Additional QA/QC and post-processing are warranted as part of automated data analysis (e.g., An et al., 2017).

### 4.3 Emergency management

Vanuatu is an island nation in the Southwest Pacific with an 800-900 km long archipelago of 83 islands. The Vanuatu Meteorology and Geohazards Department (VMGD) is the government institute with the mandate to monitor meteorological and geological hazards, including volcanoes, earthquakes, and tsunamis, and provide early warning updates to the public. VMGD has an established geological monitoring network consisting of 15 plus seismic monitoring stations scattered along the six provinces of Vanuatu. Broadband sensors and established telemetry transmission to the VMGD data center enables near real time detection of seismic events ~~detection.~~ The installation of tide gauges near the coastline of some islands assists with tsunami monitoring. However, the detection range is locali~~z~~sed to Vanuatu region and does not extend regionally or to the subduction zone.

The National Disaster Management Office (NDMO) is responsible for the response and recovery ~~to~~ from any disaster and activation of the National Emergency Operations Center with the advice from VMGD. Having a well-established hierarchy of groups down to province and community levels allow~~s~~ coordinated pre-disaster awareness and outreach efforts and transfer of response and recovery efforts to the government and partners post disaster. The effectiveness of preparedness and mitigation measures developed ~~is~~ are a result of ~~the~~ VMGD'S availability of the real-time seismic and historical data ~~possessed by VMGD~~. The latter is now augmented here by synthetic seismic and tsunami data from three recent major earthquakes and tsunamis as well as the UNESCO-IOC maximum scenario along with its subevents for hazard assessment and long-term planning.

The deployment of the Tamtam SMART cable and integration of its real-time data into VMGD's monitoring system will greatly enhance the current early warning system. The Vanuatu subduction zone has so far been lacking direct observation since there has never been monitoring equipment installed in the area. The seismic, temperature and pressure data that will be made available by the four proposed ASN Climate Change Nodes will feed additional information to the current system providing earthquake detection parameters and tsunami threat analysis in and around the subduction zone. Acquiring such data will support preparedness and mitigation efforts developed by NDMO, resulting in a well informed and prepared country. The benefits will extend to the southwest Pacific and will be of great interest to the research community as well.

*Code availability.* The NEOWAVE code for tsunami modeling may be requested from the corresponding author for academic research. The SYNGINE seismic wave simulator is available online (https://ds.iris.edu/ds/products/ondemandsynthetics/).

*Data availability.* The digital elevation model used in this study is available at GEBCO (https://www.gebco.net/data_and_products/gridded_bathymetry_data/).

*Authorship contribution.* KC: Conceptualization, Methodology, Investigation, Project Administration, Writing - original draft, review and editing. YY: Methodology, Investigation, Software, Formal analysis, Data curation, Visualization, Writing - review and editing. TL: Methodology, Investigation, Software, Formal analysis, Data curation, Visualization, Writing - original draft review and editing. MF: Writing - original draft, review and editing. JN: Writing - original draft, review and editing. BH: Writing - review and editing.

*Declaration of competing interest.* The authors declare that they have no known competing financial interests or personal relationships that could have appeared to influence the work reported in this paper.

*Acknowledgements.* SOEST Contribution No. XXXXX.

*Financial support.* The Gordon and Betty Moore Foundation funded this study through Grant No. GBMF10787 to the University of Hawaii and subawards to Subsea Data Systems and Vanuatu Meteorology and Geo-hazards Department. T. Lay was supported by the National Science Foundation under grant number EAR-1802364.

## References

An, C., Cai, C., Zheng, Y., Meng, L, Liu, P.: Theoretical solution and applications of ocean bottom pressure induced by seismic seafloor motion. Geophys. Res. Lett., 44, 10,272-10,281, doi:10.1002/2017GL075137, 2017.

Aranguiz, R., Catalán, P.A., Cecioni, C., Bellotti, G., Henriquez, P., and González, J. Tsunami resonance and spatial pattern of natural oscillation modes with multiple resonators. J. Geophys. Res.: Oceans, 124, 7797-7816, doi:10 .1029/2019JC015206, 2019.

Bai, Y., Liu, C., Lay, T., Cheung, K.F., and Ye, L.: Optimizing a model of coseismic rupture for the 22 July 2020 Mw 7.8 Simeonof earthquake by exploiting acute sensitivity of tsunami excitation across the shelf break. J. Geophys. Res.: Solid Earth, 127, e2022JB024484, doi:10.1029/2022JB024484, 2022.

Bai, Y., Liu, C., Lay, T., Cheung, K.F., and Yamazaki, Y.: Fast and slow intraplate ruptures during the 19 October 2020 magnitude 7.6 Shumagin earthquake. Nat. Comm., 14(1), 2015, doi:10.1038/s41467-023-37731-2, 2023.

Bai, Y., Yamazaki, Y, and Cheung, K.F.: Intercomparison of hydrostatic and nonydrostatic modeling for tsunami inundation mapping. Phys. Fluids, 35(7), 077111, doi:10.1063/5.0152104, 2023b.

Cheung, K.F., Bai, Y., and Yamazaki, Y.: Surges around the Hawaiian Islands from the 2011 Tohoku tsunami. J. Geophys. Res. Oceans, 118(10), 5703-5719, doi:10.1002/jgrc.20413, 2013.

Cleveland, K.M., Ammon, C.J., and Lay, T.: Large earthquake processes in the northern Vanuatu subduction zone, *J. Geophys. Res.: Solid Earth*, 119, 8866-8883, doi:101002/2014JB011289, 2014.

Davies, G. and Griffin, J.: The 2018 Australian Probabilistic Tsunami Hazard Assessment. Record 2018/41, Geoscience Australia, Canberra, https://doi.org/10.11636/Record.2018.041, 2018.

https://doi.org/10.5194/egusphere-2025-5825
Preprint. Discussion started: 11 December 2025

Dziewonski, A.M. and Anderson, D.L.: Preliminary reference Earth model. Phys. Earth Planet. Int., 25, 297-356, doi:10.1016/0031-9201(81)90046-7, 1981

Fry, B., McCurrach, S.-J., Gledhill, K., Power, W., Williams, M., Angove, M., Arcas, D. and Moore, C.: Sensor network warns of stealth tsunamis. Eos, 101, doi:10.1029/2020EO144274, 2020.

Heidarzadeh, M., Harada, T., Satake, K., Ishibe, T., and Gusman, A.R.: Comparative study of two tsunamigenic earthquakes in the Solomon Islands: 2015 $M_W$ 7.0 normal-fault and 2013 Santa Cruz $M_W$ 8.0 megathrust earthquakes. Geophys. Res. Lett., 43(9), 4340-4349, doi:10.1002/2016GL068601, 2016.

Howe et al.: SMART cables for observing the global ocean: science and implementation. Front. Earth Sci., 6, 424, doi:10.3389/fmars.2019.00424, 2019.

Howe et al.: SMART subsea cables for observing the earth and ocean, mitigating environmental hazards, and supporting the blue economy. Front. Earth Sci., 9, 775544, doi:10.3389/feart.2021.775544, 2022.

Lay, T., Ye, L., Kanamori, H., Yamazaki, Y., Cheung, K.F., and Ammon, C. J.: The February 6, 2013 $M_W$ 8.0 Santa Cruz Islands earthquake and tsunami. Tectonophysics, 608, 1109–1121, doi:10.1016/j.tecto.2013.07.001, 2013.

Li, L. and Cheung, K.F.: Numerical dispersion in non-hydrostatic modeling of long-wave propagation. Ocean Modell., 138, 68-87, doi:10.1016/j.ocemod.2019.05.002, 2019.

Ioualalen, M., Pelletier, B., and Solis Gordillo, G.: Investigating the March 28th 1875 and the September 20th 1920 earthquakes/tsunamis of the Southern Vanuatu arc, offshore Loyalty Islands, New Caledonia. Tectonophysics, 709, 20–38, doi:j.tecto.2017.05.006, 2017.

Okada, Y.: Surface deformation due to shear and tensile faults in a half-space. Bull. Seismol. Soc. Am., 75(4), 1125-1154, doi:10.1785/BSSA0750041135, 1985.

Paris, R, Pelletier, B., Roger, J., Wassmer, P., and Sabatier, P.: Sedimentary evidence of tsunamis in New Caledonia, southwest Pacific. Mar. Geol., 463, 107116, doi:10.1016/j.margeo.2023.107116, 2013.

Robert, W.H., Yamazaki, Y., Cheung, K.F., and Lay, T.: Tsunami variability for the 2021 megathrust and 2023 outer rise $M_W$ 7.7 earthquake southeast of the Loyalty Islands. J. Geophys. Res.: Oceans, 130, e2024JC021880, doi:10.1029/2024JC021880, 2025.

Roger, J. and Pelletier, B.: A brief history of tsunamis in the Vanuatu Arc. Nat. Haz. Earth Syst. Sci., 24(10), 3461-3478 doi:10.5194/nhess-24-3461-2024, 2024.

Roger, J.H.J., Pelletier, B., Duphil, M., Lefévre, J., Aucan, J., Lebellegard, P, Thomas, B. Bachelier, D., and Varillon, D.: The *Mw* 7.5 Tadine (Maré, Loyalty Islands) earthquake and related tsunami of 5 December 2018: seismotectonic context and numerical modeling. Nat. Haz. Earth Syst. Sci., 21(11), 3489-3508, doi:10.5194/nhess-21-3489-2021, 2021.

Tanioka, Y. and Satake, K.: Tsunami generation by horizontal displacement of ocean bottom. Geophys. Res. Lett., 23(8), 861-864, doi:10.1029/96GL00736, 1996.

UNESCO-IOC: Expert Meeting on Tsunami Sources, Hazards, Risk and Uncertainties Associated with the Vanuatu, Solomon and New Britain Subduction Zones, Port Vila, Vanuatu, 14-17 May 2024. Workshop Report 315, UNESCO, Paris, France. https://unesdoc.unesco.org/ark:/48223/pf0000392442.locale=en, 2025.

World Bank: Global Rapid Post-Disaster Damage Estimation Report: The December 17, 2024 Mw 7.3 Earthquake in Port Vila, Vanuatu. Global Facility for Disaster Reduction and Recovery, World Bank, Washington, DC, http://hdl.handle.net/10986/42820, 2025.

Yamazaki, Y., Bai, Y., Goo, L.L., Cheung, K.F., and Lay, T.: Nonhydrostatic modeling of tsunamis from earthquake rupture to coastal impacts. J. Hydraul. Eng., 149(9), 04023033, doi:10.1061/JHEND8.HYENG-133, 2023.

Yamazaki, Y., Cheung, K.F., and Kowalik, Z.: Depth-integrated, non-hydrostatic model with grid nesting for tsunami generation, propagation, and run-up. Int. J. Numer. Meth. Fluids, 67, 2081-2107, doi:10.1002/fld.2485, 2011.

Yamazaki, Y., Kowalik, Z., and Cheung, K.F.: Depth-integrated, non-hydrostatic model for wave breaking and run-up. Int. J. Num. Meth. Fluids, 61, 473-497, doi:10.1002/fld.1952, 2009.

Ye, L., Gong, W., Lay, T., Kanamori, H., and Chen, X.: Shallow megathrust rupture during the 10 February 2021 *Mw* 7.7 Southeast Loyalty Islands Earthquake Sequence. Seism. Rec., 1(3), 154–163, doi:10.1785/0320210035, 2021.